Investigating new symmetry classes in magnetorheological elastomers: cantilever bending behavior

2011 Smart Mater. Struct. 20 105022

(http://iopscience.iop.org/0964-1726/20/10/105022)

Smart Mater. Struct. **20** (2011) 105022 (10pp) doi:10.1088/0964-1726/20/10/105022

Investigating new symmetry classes in magnetorheological elastomers: cantilever bending behavior

P von Lockette[1], S E Lofland[2], J Biggs[1], J Roche[1], J Mineroff[1] and M Babcock[1]

[1] Department of Mechanical Engineering, Rowan University, 201 Mullica Hill Road, Glassboro, NJ 08028, USA
[2] Department of Physics and Astronomy, Rowan University, 201 Mullica Hill Road, Glassboro, NJ 08028, USA

E-mail: vonlockette@rowan.edu

Received 20 December 2010, in final form 29 June 2011
Published 12 September 2011
Online at stacks.iop.org/SMS/20/105022

Abstract
This work defines and examines four classes of magnetorheological elastomers (MREs) based upon permutations of particle alignment–magnetization pairs. Particle alignments may either be unaligned (e.g. random) or aligned. Particle magnetizations may either be soft-magnetic or hard-magnetic. Together, these designations yield four material types: A–S, U–S, A–H, and U–H. Traditional MREs comprise only the A–S and U–S classes. Samples made from 325-mesh iron and 40 μm barium hexaferrite powders cured with or without the presence of a magnetic field served as proxies for the four classes. Cantilever bending actuating tests measuring the magnetically-induced restoring force at the cantilever tip on 50 mm $\times$ 20 mm $\times$ 5 mm samples yielded $\sim$350 mN at $\mu_0 H = 0.09$ T for classes A–H, A–S, and U–S while class U–H showed only $\sim$40 mN. Furthermore, while classes U–S and A–S exerted forces proportional to tip deflection, they exerted no force in the undeformed state whereas class A–H exerted a relatively constant tip force over its entire range of deformation. Beam theory calculations and models with elastic strain energy density coupled with demagnetizing effects in the magnetic energy density were used to ascertain the magnitude of the internal bending moment in the cantilever and to predict material response with good results. This work highlights the ability of the newly developed A–H MRE materials, and only that material class, to operate as remotely powered bidirectional actuators.

(Some figures in this article are in colour only in the electronic version)

1. Introduction

The study of magnetorheological elastomers (MREs) as a viable class of smart materials has gained increasing interest since they have recently exhibited large magnetorheological (MR) effects in sample materials [1–14]. The MR effect in shear ΔG is the relative change in a material's complex modulus G when placed within a magnetic field $\mathbf{H}$ with respect to the modulus with no field present, i.e.

$$\Delta G = \frac{G(H) - G(H = 0)}{G(H = 0)}. \quad (1)$$

This change in stiffness has been utilized in the design of several tunable/controllable vibration isolation devices [15–27]. Beyond this work, however, the authors know of no studies of MRE materials that examine their ability to act as remotely powered actuators.

MREs are fabricated by combining magnetic particles with an uncured elastomer compound such as natural or silicone rubber. Effective particle sizes range from nanoparticles to coarse ($\sim$500 μm) Fe filings [8]. Within the matrix, filler particles can either be distributed randomly or have some regular alignment producing either an isotropic or anisotropic medium, respectively. Previous work on

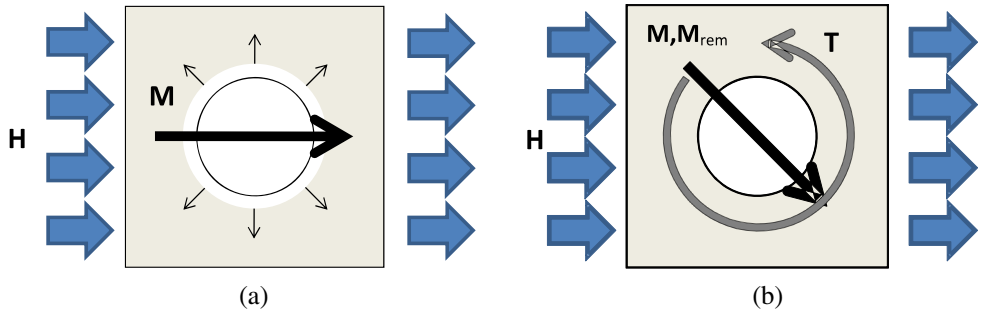

Figure 1. (a) Soft-magnetic particles, which have no preferred magnetic orientation (small arrows), when exposed to a uniform magnetic field **H** will have magnetization, **M** (dark arrow), aligned with the external field. (b) Hard-magnetic particles with remanent magnetization $\mathbf{M}_{rem}$ will ideally have **M** remain aligned with the axis of $\mathbf{M}_{rem}$ which is local to the particle and thus allows for the generation of magnetic torque **T**.

Fe-based MREs has led to the belief that $\mu_0 H \sim$ 1–2 T applied during curing tends to create chains of aligned particles within the matrix which affect behavior; in some instances the maximal MR effect has been increased by up to 40% in aligned samples over unaligned samples having the same particle volume fraction [6–8, 12]. However, these aligned chains exist predominantly for materials with particle volume fractions below 20% [28].

Previous works have focused solely on the use of soft-magnetic particles, such as Fe, embedded in the elastomer matrix to produce MRE materials. In contrast, this work examines hard-magnetic particles as well, comparing differences in behavior between what are termed S-MRE materials, those made from embedded soft-magnetic particles, and H-MRE materials, those made from embedded hard-magnetic particles. The difference is critically important because the two materials are driven by distinctly different responses to magnetic fields.

In magnetically soft materials, in the absence of shape anisotropy, the magnetization **M** of the particles remains parallel to **H** (figure 1(a)). Thus there is no net force or torque acting on spherical particles within a uniform field if the composite is unperturbed with respect to that field. When chains of particles are sheared within the field, individual particle magnetizations still align with **H**; however, demagnetizing effects between particles generate a restoring torque that seeks to minimize the energy of the system by returning particles to their unperturbed state (see, for example, Shen *et al* [10] for a derivation of this restoring force which is ultimately linear with respect to the shear strain).

In ideal H-MREs the particles have a value of **M** that remains constant with respect to the local coordinate system of each particle (figure 1(b)). The fundamental difference between S-MREs and H-MREs lies in the torque generated by **H** within the H-MRE's embedded particles, which in turn affects the bulk material *en masse*. The magnetic torque density **T** within the particles themselves is determined by $\mathbf{T} = \mathbf{M} \times \mathbf{H}$. Consequently, in contrast to S-MREs, in the unperturbed state H-MREs can generate substantial torques. Thus, H-MREs can be more accurately described as active materials as opposed to reactive S-MREs.

While previous works have examined many aspects of MRE behavior including particle alignments, none has yet

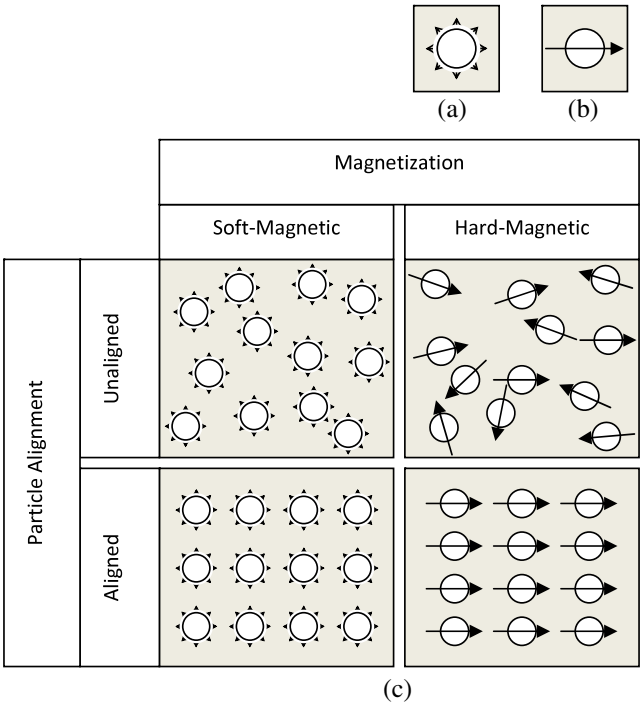

Figure 2. Iconography of (a) soft-magnetic and (b) hard-magnetic particles, and (c) schematics of four classes of MREs based on alignment–magnetization permutations.

examined the role of hard- versus soft-magnetic material behavior on MRE response. Thus, we have investigated these two magnetic property categories, soft-magnetic (S), which is isotropic in magnetic response and hard-magnetic (H), which is anisotropic (figures 2(a) and (b)). Note that in this figure the single arrow of the hard-magnetic material highlights its preferred magnetization axis while the magnetically soft material is drawn as an arrowed-circle to show that it has no preferred magnetization direction. The orientation and spatial distribution of filler particles also fall into two categories: unaligned (U) materials which are cured in zero field and aligned (A) materials which are cured in a high magnetic field. Permutations of these definitions lead to the four possible classes shown in figure 2(c), namely A–H, A–S, U–H, and U–S, and are examined in the present work. It

bears mentioning that though the notion of particle alignment has paradigmatically assumed the formation of chain-like structures, a more recent work has shown that the degree of alignment in MREs cured in a magnetic field is dependent on both the particle volume fraction and the strength of the curing field [28].

2. Experimental methods

2.1. Sample preparation

MRE materials made with barium M-type hexaferrite (BaM) and Fe powders, aligned and unaligned, served as proxies for each of the four classes in this work. Samples were fabricated by curing DOW HS II silicone elastomer compound mixed with 30% by volume of either nominally 40 μm BaM or 325-mesh (<40 μm) iron (Fe) particles in aluminum molds. BaM with a coercive field of $\mu_0 H_c > 0.4$ T, provided the hard-magnetic behavior while Fe with $\mu_0 H_c < 2.5$ mT served as the soft-magnetic case. The molds were sized to fabricate sheets measuring 130 mm × 75 mm × 5 mm. Material classes A–H and A–S were produced by curing in $\mu_0 H \sim 2$ T along the direction normal to the sheet, while the other classes were cured in ambient field. From these sheets smaller samples were cut and used for testing.

Samples measuring 75 × 20 × 5 mm^3 were prepared for a cantilever bending experiment; 50 mm was the free cantilever length. A C-shaped electromagnet capable of generating $\mu_0 H$ up to 0.15 T was used for testing in the configuration depicted in figure 3. A procedure was developed to compare the actuation capabilities of all four classes, including materials that did not deform freely under a magnetic field. In this experiment, increasing deflections were imposed on the tip of the sample while the resulting restoring force acting against the deflector, the force that tended to return the sample to its undeformed state, was measured versus magnetic field strength. A schematic of this testing procedure can be seen in figure 3 that highlights the field direction (arrow outlines), the poling direction (if present) of the MRE (line arrows) and the force and displacement measurements, P and Δ, respectively. In these experiments, the force transducer remains in rigid contact with the sample tip during the entire experiment. A Shimpo model FGV-0.5× force gauge with a non-magnetic extension was used to induce the displacement on each of the samples as well as to measure the force generated. The transducer's stiffness was sufficiently high that the mN forces measured caused negligible strain within the transducer and extension with respect to the measured displacements.

The magnetization of the samples was measured with a Lakeshore 7300 vibrating sample magnetometer to estimate the volume fractions of magnetic material present, to determine the magnetic susceptibility and to ascertain the alignment of magnetic particles in samples which were cured in a field. Remanent magnetization M_{rem} for the A–H cases was $M_{rem} = 103 \times 10^5$ A m^{-1} and 28×10^5 A m^{-1} parallel and perpendicular to the magnetizing direction, respectively. This compares to a saturation magnetization $M_{sat} = 128$ A m^{-1}, which is in accord with the 30 ± 1 vol% of BaM, suggesting

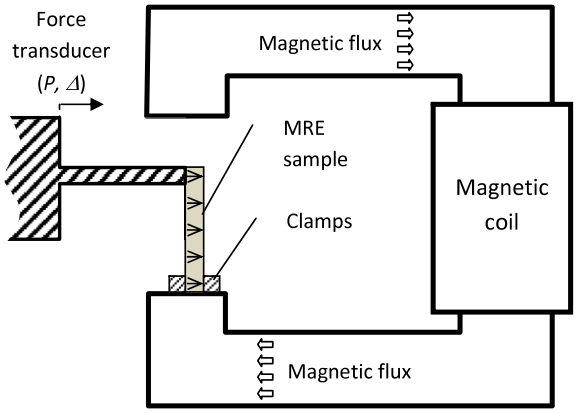

Figure 3. Experimental setup of forced displacement testing showing magnetic coil with flux direction. A non-ferrous extension to the force gauge proscribed displacement and recorded the resisting load. The MRE poling direction, if present, is shown by arrows in the sample.

that most of the particles were aligned. Both the S-MRE U–S and A–S materials showed $M_{rem} \sim 0$ as expected for soft-magnetic materials. Saturation magnetizations were $M_{sat} =$ 1.7–1.8 MA m^{-1}, also consistent with 30 ± 1 vol% of Fe.

2.2. Forced displacement cantilever bending

To begin, all four classes were assumed to follow the general superposition of magnetic and elastic contributions to the total force exerted by the material:

$$F_T(\Delta, H) = F_E(\Delta) + F_H(\Delta, H) \quad (2)$$

where Δ is the tip displacement, $F_T(\Delta, H)$ is the field- and displacement-dependent total force recorded by the transducer, $F_H(\Delta, H)$ is the field- and displacement-dependent force exerted by the sample due to magnetic interactions, and $F_E(\Delta)$ is the force exerted by the sample due to its inherent elasticity which depends solely on its own state of deformation as measured by tip displacement.

Setting the applied magnetic field to zero leaves $F_T(\Delta, 0) = F_E(\Delta)$. Inherent in this simplification is the well warranted assumption $F_H(\Delta, 0) = 0$ for all Δ, i.e. with no applied magnetic field there can be no net magnetic force generated at the deflector. This is especially true of S-MRE materials which have $M_{rem} = 0$. However, in H-MRE materials the $H = 0$ (zero applied field) response contains an inherent 'magnetic stiffness' beyond the elastic response that cannot be avoided since in H-MRE remanent magnetizations are non-zero. Consequently, in this work F_H is defined from the response at magnetic field beyond that of F_E, the response with no externally applied field present. Tests were run for each class at zero field to determine F_E versus Δ. The same experimental procedure was followed under the presence of an external magnetic field. Tests were run as $\mu_0 H$ varied up to 0.09 T. Larger field strengths caused portions of the sample to deform outside the applied magnetic field.

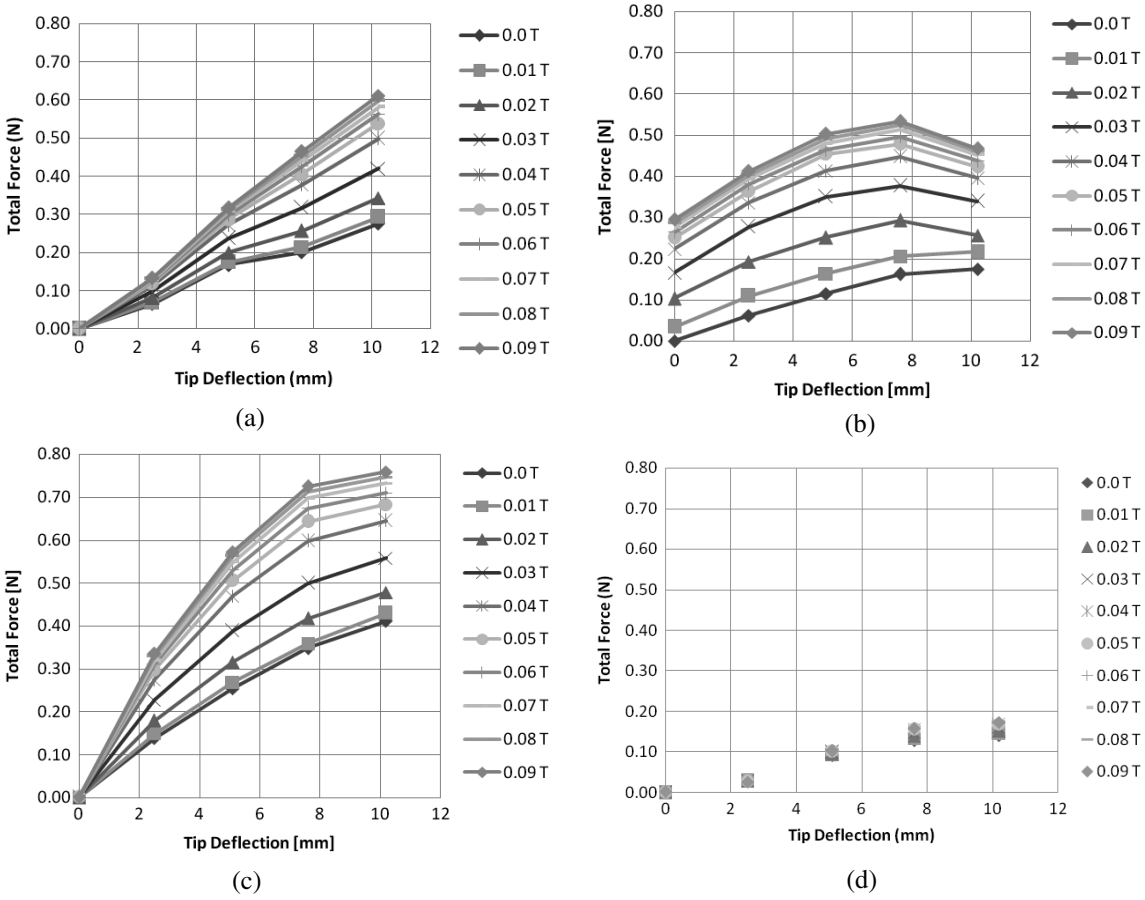

Figure 4. Total force as a function of tip deflection for (a) class A–S, (b) class A–H, (c) class U–S, and (d) class U–H. All forces generally increase with field strength and tip deflection; however, for class A–H, there are non-zero forces even at zero deflection.

3. Results of cantilever bending experiments

3.1. Force versus deflection

$F_T(\Delta, H)$ as a function of tip deflection is shown in figure 4 for all four classes. Both S-MRE samples (A–S and U–S materials) show no force at zero deflection for all field strengths while the A–H H-MRE material shows increasing tip force at zero deflection as H is increased. The H-MRE type U–H material shows zero force at zero deflection but almost no change in tip force as H is increased. All samples show a positive slope with respect to tip deflection, an expected result of the elastic behavior.

Subtracting F_E for a given material (zero-field curve in each graph) from the remaining data for that material yields F_H, from equation (2),

$$F_H(\Delta, H) = F_T(\Delta, H) - F_E(\Delta) \tag{3}$$

as a calculated quantity dependent on sets of experimental data with and without the presence of a magnetic field. These data for F_H are presented in figure 5.

Figure 5(a) shows the magnetic force versus tip deflection for an A–S S-MRE sample for various fields. The data show a relatively linear behavior with tip deflection (remembering that the elastic behavior has been subtracted out) for all field strengths and increasing force with increasing field strength for a given tip deflection. Most notably, the A–S material generates no magnetic force at zero tip deflection for all field strengths tested. The tip forces reach a maximum of 0.34 N at the final 10 mm tip deflection.

Figure 5(b) shows the results of a type A–H (H-MRE) material. The tip forces generated clearly increase with increasing field strength as in the A–S material. However, in contrast to the A–S material, the A–H material shows increasing tip forces with increasing field strength even at zero tip deflections. The lower field strengths seem to generate constant-valued forces across tip deflection while the higher field strengths reach a maximum of 0.38 N at an intermediate deflection of 5 mm.

Figure 5(c) shows the S-MRE type U–S material. Similar to the class A–S material, these tests show an initially linear behavior with respect to tip deflection; however, the response begins to saturate near 5 mm of deflection. The tip force is zero at zero deflection for all field strengths as in the type A–S case. The maximum tip force generated is 0.37 N at 7.5 mm.

Figure 5(d) shows the behavior of the H-MRE type U–H material. Class U–H is unique in that it has the poorest actuation behavior, showing no response for all field strengths for tip deflections below 5 mm and only marginal increases in tip force with field strength at the highest tip deflections. The

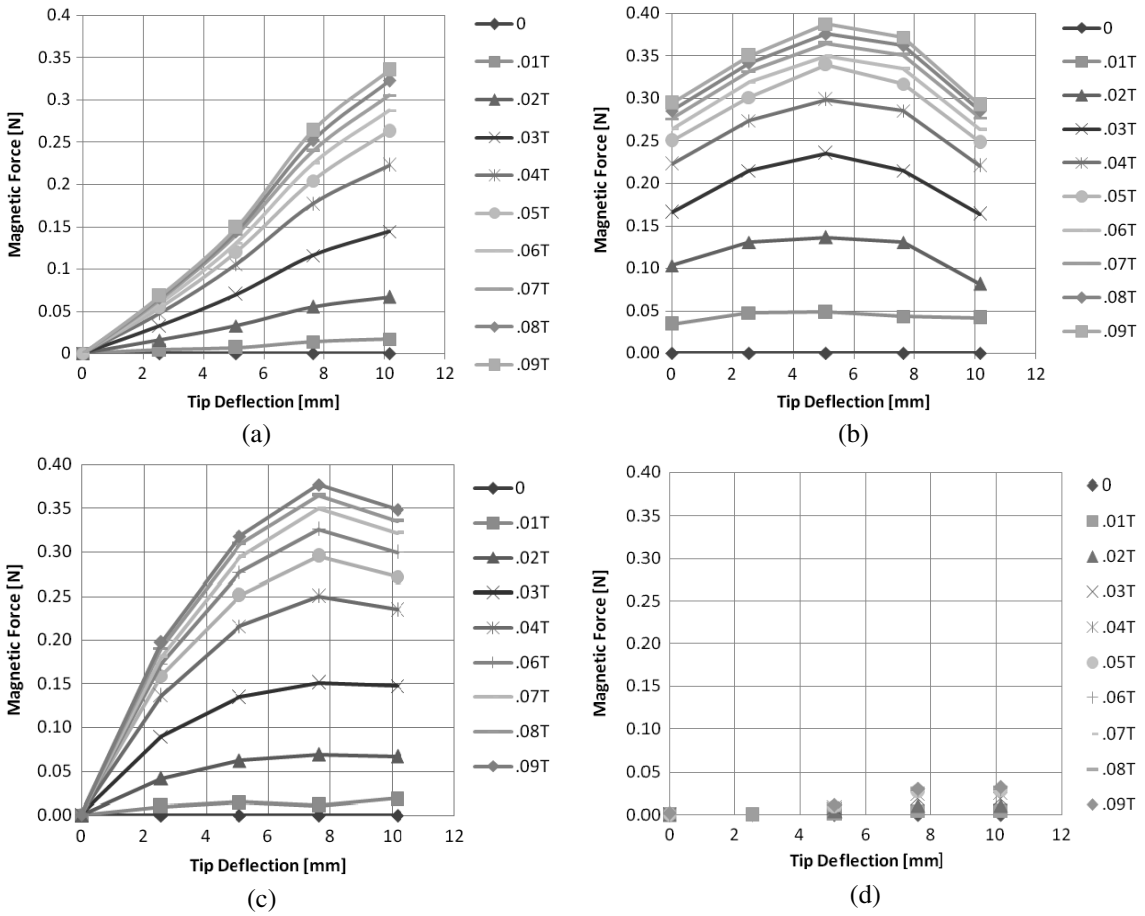

Figure 5. Magnetic force as a function of tip deflection data for (a) class A–S, (b) class A–H, (c) class U–S, and (d) class U–H. Forces for classes A–S and U–S are initially linear with respect to displacement and scale with the field. Class A–H is the only class capable of exerting force at zero tip deflection while forces in class U–H are significantly smaller than those of other classes.

maximum tip force generated, 0.004 N, is less than 10% of type A–H, the other H-MRE sample.

3.2. Work potential

The preceding data allow calculation of the magnetic work potential, W_{H}, of each sample throughout the testing. The magnetic work potential at a given field strength and tip deflection is defined as

$$W_{\mathrm{H}}(H) = \int_0^{\upsilon_{\max}} F_{\mathrm{H}}(\Delta, H)\,\mathrm{d}\Delta \tag{4}$$

for fixed H. This expression yields the amount of magnetic work each sample could perform at a given field strength as the internal magnetic actuation retracts the tip from $\upsilon_{\max}$ to 0 mm against a resistance. These results are summarized in figure 6.

Sample A–H, in which the highest force was seen, generates a maximum of 3.56 mJ of work. Sample A–H shows the maximum values of work capability due to its ability to generate forces at zero deflection, something no other class is capable of. Sample U–S showed the second highest value of work done with 2.71 mJ, 76% of the maximum seen in class A–H. Significantly lower than that class A–S produces 1.65 mJ of work done, 46% of the class A–H value. Sample U–H, which generated no significant forces during testing, is only capable of producing a maximum of 0.14 mJ of work, only ∼4% of the work capability of class A–H, the other H-MRE material tested. Each material shows initial increases in work potential as field strength is increased but eventually begins to saturate, beginning near $\mu_0 H = 0.04$ T.

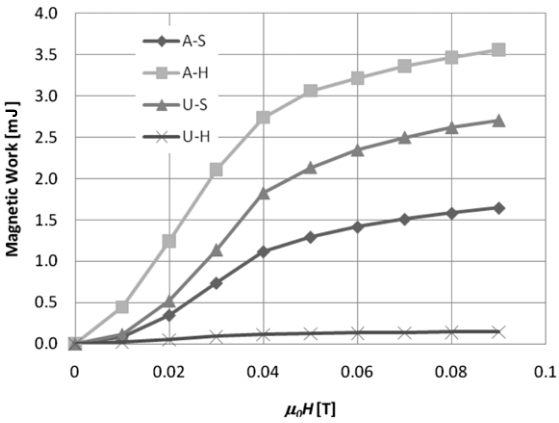

Figure 6. Magnetic work done as a function of field for all four classes.

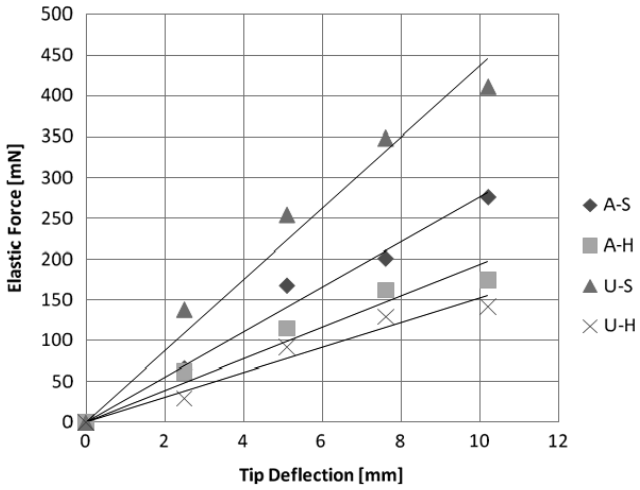

Figure 7. Deflection as a function of tip displacement at zero field for all four classes, yielding the elastic compliance, κ.

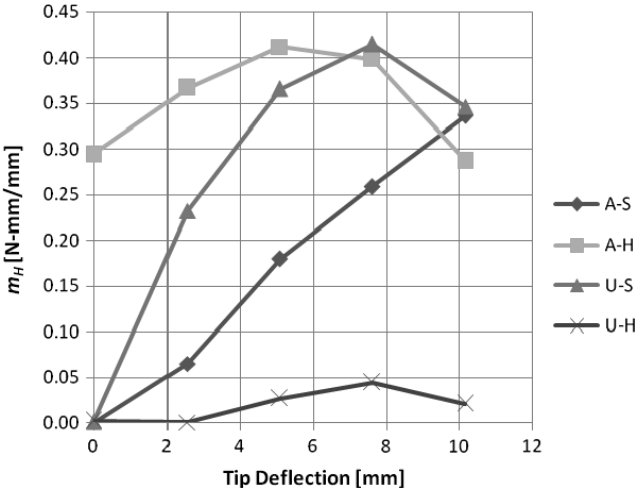

Figure 8. Calculated distributed magnetic moment in all four classes for $\mu_0 H = 0.09$ T. Lines are drawn as guides to the eye.

4. Discussion

It is useful at this point to employ Bernoulli–Euler beam theory to aid discussion of the observed behavior, though the limitations of this approach for the materials in question are well understood. Large deformations, hyperelastic matrix behavior, field-dependent moduli, locally non-uniform magnetic fields in a magnetoelastic composite, etc are all present in this case which nominally preclude predictions using simple beam theory. However, the results derived herein provide useful metrics with which to compare across experiments while at the same time capturing aspects of the underlying MRE response. In addition, results of the analysis highlight the utility of the approach at this stage.

Bernoulli–Euler beam theory states the deflection $v(x)$ of the neutral axis in a long slender beam of length L and moment of inertia I is governed by

$$\frac{\mathrm{d}^2 v(x)}{\mathrm{d}x^2} = \frac{T}{EI} \tag{5}$$

where T is the internal bending moment in the beam, I is its second moment of inertia, and E is its modulus of elasticity. For a cantilever beam built-in at $x = L$ and loaded transversely at $x = 0$ by a force P, it can be shown that $T(x) = Px$, from which it follows from equation (5) that $v_{\max} = P/\kappa$, where $\kappa = 3EI/L^3$ is an elastic bending stiffness. The maximum deflection occurs at $x = 0$.

Next, consider the same beam under the influence of some distributed, constant, counterclockwise moment per unit length m_{H} without the end-load P. At this point in the analysis, this moment is ascribed to the interaction of the embedded particles with the external magnetic field in a similar fashion in both S-MRE and H-MRE materials. The internal moment at any cross-section of the beam is then given by

$$T(x) = -x m_{\mathrm{H}}, \tag{6}$$

which yields the solution $v_{\max} = -m_{\mathrm{H}}/\kappa$ where κ is the elastic bending response determined previously.

The principle of superposition states that the solution to the combined loading case of the end-load P (herein both elastic and magnetic contributions to the force) and the distributed magnetic moment m_{H} is the sum of the solutions to each problem individually such that

$$v_{\max} = (P - m_{\mathrm{H}})/\kappa. \tag{7}$$

In the cantilever bending test setup (figure 3), the force transducer provided the transverse force P while the magnetic field–particle interactions, regardless of their exact nature, provided an effective distributed magnetic moment m_{H} yielding the total tip displacement of equation (7). Given experimental data for tip deflection, $v_{\max} = \Delta$, measured values of $P = F_{\mathrm{T}}(\Delta, H)$, and experimentally determined values for κ (the slope of the zero-field curves in figure 4), the distributed moment m_{H} for each class of material as a function of field strength and tip deflection was determined from

$$m_{\mathrm{H}} = P - \kappa v_{\max}. \tag{8}$$

The bending stiffness results of each class of material are compared in figure 7 with the slopes of the curves yielding κ directly. The data show linear behavior initially for all cases while the U–H and A–H cases show signs of softening at higher deflections. Overall, the U–S and A–S (Fe) samples appear stiffer than the A–H and U–H (BaM) samples and aligned samples have stiffer responses than unaligned ones for H-MRE types. Classes U–H and A–H have $\kappa = 15.0$ and 17.7 mN mm^{-1}, respectively, while classes A–S and U–S have $\kappa = 27.0$ and 40.6 mN mm^{-1}, respectively. All linear regressions have $R^2 \geqslant 0.96$.

Figure 8 shows m_{H} as a function of $v_{\max}$, at $\mu_0 H = 0.09$ T for all four classes calculated from equation (8). The figure shows a linear response with respect to tip deflection initially in both S-MRE samples (U–S and A–S), though with different slopes, with class U–S showing a steeper response but also a reduction in bending moment beyond $v = 7.5$ mm. The U–S and A–S materials reach 0.42 and 0.35 N mm/mm, respectively, at their maxima. The figure also shows class

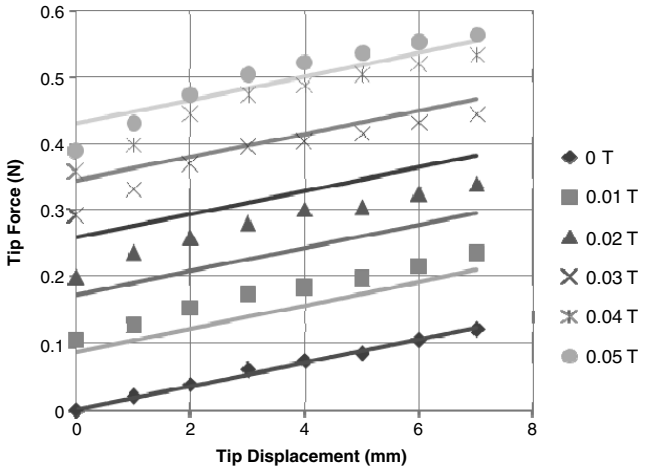

Figure 9. Tip force as a function of field and tip displacement for A–H material. The lines represent predictions made with equation (8) based on constants taken from zero field (diamonds) and zero tip displacement (y-axis) cases.

U–H developing only 0.04 N mm/mm at most, less than 10% of its class A–H counterpart. Class A–H shows a high bending moment and, most notably, its value begins at $m = 0.30$ N mm/mm, increases to 0.42 N mm/mm, and decreases to 0.29 N mm/mm, never approaching zero as do the A–S and U–S (S-MRE) cases.

The data in conjunction with the model support our claims that m_{H} is relatively independent of displacement in H-MREs (as compared to S-MREs) and linearly varying with displacement in S-MREs, and that in both materials m_{H} increases with applied field. For further validation, the model was used to predict the arbitrary tip force–deflection-field response of a second set of cantilever A–H H-MRE specimens with only two tests to characterize two parameters: the fully elastic behavior as exhibited by the elastic bending stiffness κ and a field-dependent magnetic response, defined from $m_{\mathrm{H}} = \eta H$ where η is the slope of the m_{H} as a function of H curve from equation (8) for $v_{\max} = 0$. The parameter η stems from the rise in P as field is increased (shown along the y-axis in figure 4(b)). The specimens were cut to the same dimensions as the previous set and used in the same experimental setup.

The P versus $v_{\max}$ behavior from 0 to 7 mm in displacement at zero field yielded $\kappa = 17.6$ mN mm^{-1} ($R^2 = 0.992$, data not shown) from equation (7) with $m_{\mathrm{H}} = 0$. Similarly, a test keeping $v_{\max} = 0$ while increasing $\mu_0 H$ from 0 to 0.05 T, showed $\eta = 9.46$ N mm/mm T ($R^2 = 0.963$, data not shown). Results of predictions (lines) are compared to data (symbols) in figure 9. The zero displacement data (symbols along the y-axis from the origin) and the zero applied field data (bottom row of symbols, diamonds) represent the data used for characterization, while the intermediate curves represent model predictions. The results show good agreement with no adjustable parameters, though the linearized dependence on field strength does not adequately capture magnetization behavior.

Modeling the effects of the magnetic field on the cantilever as a generalized distributed moment works well as a phenomenological approach; however, it further highlights the fundamental differences in behavior between S- and H-MREs. While H-MREs are arguably driven by magnetic torques acting on individual particles S-MREs are not, instead relying on demagnetizing effects to provide a restoring force.

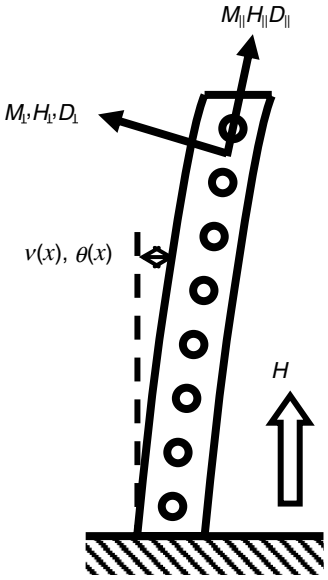

Figure 10. Schematic of the cantilever beam showing the nominally aligned particles, parallel and perpendicular component directions of the magnetic field **H**, magnetization **M**, and demagnetizing tensor **D**, transverse bending deflection $v(x)$ and deflection angle $\theta(x)$.

To model S-MREs more accurately, an energy approach may be employed to model the elastic energy of the beam in an end-loaded cantilever bending mode combined with the energy of particle magnetization due to the applied field plus additional demagnetizing effects within the soft-magnetic particles. The demagnetizing effects are dependent on both particle shape and particle geometry.

The linear magnetic energy density U_{H} is given as [29]

$$U_{\mathrm{H}} = \mu_0\left(\tfrac{1}{2}\mathbf{M}\cdot\mathbf{H}A + \tfrac{1}{2}\mathbf{M}\overleftrightarrow{\mathbf{D}}\cdot\mathbf{M}A\right) \tag{9}$$

where A is the cross sectional area of the cantilever and $\overleftrightarrow{\mathbf{D}}$ is the demagnetizing tensor. For the present beam, which is effectively a sheet, the only non-negligible element of $\overleftrightarrow{\mathbf{D}}$ is normal to the surface, which must be 1 since $\mathrm{Tr}\,\overleftrightarrow{\mathbf{D}} = 1$. Consequently, in the $\|- \perp - z$ coordinate system local to the cantilever's surface the demagnetizing tensor is given by

$$\overleftrightarrow{\mathbf{D}} = \begin{bmatrix} 0 & 0 & 0 \\ 0 & 1 & 0 \\ 0 & 0 & 0 \end{bmatrix} \tag{10}$$

where figure 10 shows the orientations of the parallel and perpendicular components of the internal magnetization **M**, demagnetization tensor **D** and **H**.

The magnetization of the composite can then be written as components parallel and normal to the surface, $M_{\|}$ and $M_{\perp}$, respectively. Noting the local magnetic field $\mathbf{H}_{\mathrm{loc}}$ is given by $\mathbf{H}_{\mathrm{loc}} = \mathbf{H} - \overleftrightarrow{\mathbf{D}}\cdot\mathbf{M}$ such that $\mathbf{M} = (\mathbf{H} - \overleftrightarrow{\mathbf{D}}\cdot\mathbf{M})\bar{\chi}$, where $\bar{\chi}$ is the effective magnetic susceptibility of the composite, one finds

$$M_{\|} = H\bar{\chi}\cos\theta \tag{11a}$$

$$M_{\perp} = \frac{\bar{\chi}}{1+\bar{\chi}} H \sin\theta, \tag{11b}$$

where θ is the angle between the field and the beam surface, leading to

$$U_{\mathrm{H}} = \mu_0 \left[+\frac{1}{2}\bar{\chi} H^2 \cos^2\theta + \frac{1}{2}\frac{\bar{\chi}}{1+\bar{\chi}} H^2 \sin^2\theta + \frac{1}{2}\left(\frac{\bar{\chi}}{1+\bar{\chi}} H \sin\theta\right)^2 \right] A. \tag{12}$$

Assuming the small angle approximation, $(\frac{\mathrm{d}v}{\mathrm{d}x}) \sim \theta$, yields the following deformation-dependent approximation to the magnetic energy:

$$U_{\mathrm{H}} = \mu_0 \left\{ \frac{1}{2}\bar{\chi} H^2 \left[1 - \left(\frac{\mathrm{d}v}{\mathrm{d}x}\right)^2 \right] + \frac{1}{2}\frac{\bar{\chi}}{1+\bar{\chi}} H^2 \left(\frac{\mathrm{d}v}{\mathrm{d}x}\right)^2 + \frac{1}{2}\left[\frac{\bar{\chi}}{1+\bar{\chi}} H \left(\frac{\mathrm{d}v}{\mathrm{d}x}\right) \right]^2 \right\} A. \tag{13}$$

The elastic energy in the cantilever U_{E} is given from solid mechanics as

$$U_{\mathrm{E}} = \left(\frac{EI}{2}\right)\left(\frac{\mathrm{d}^2 v}{\mathrm{d}x^2}\right)^2 - P\left(\frac{\mathrm{d}v}{\mathrm{d}x}\right). \tag{14}$$

The resulting total energy expression, $U_{\mathrm{T}} = U_{\mathrm{H}} + U_{\mathrm{E}}$, yields

$$U_{\mathrm{T}} = \mu_0 \left\{ \frac{1}{2}\bar{\chi} H^2 \left[1 - \left(\frac{\mathrm{d}v}{\mathrm{d}x}\right)^2 \right] + \frac{1}{2}\frac{\bar{\chi}}{1+\bar{\chi}} \left(\frac{\mathrm{d}v}{\mathrm{d}x}\right)^2 + \frac{1}{2}\left[\frac{\bar{\chi}}{1+\bar{\chi}} H \left(\frac{\mathrm{d}v}{\mathrm{d}x}\right) \right]^2 \right\} A + \left(\frac{EI}{2}\right)\left(\frac{\mathrm{d}^2 v}{\mathrm{d}x^2}\right)^2 - P\left(\frac{\mathrm{d}v}{\mathrm{d}x}\right). \tag{15}$$

Minimizing the energy by examining $\mathrm{d}U_{\mathrm{T}}/\mathrm{d}x = 0$ yields the governing differential equation

$$\frac{\mathrm{d}^3 v}{\mathrm{d}x^3} - \frac{\mu_0 A c H^2}{EI}\frac{\mathrm{d}v}{\mathrm{d}x} - \frac{P}{EI} = 0 \tag{16}$$

where

$$c = \frac{\bar{\chi}^3}{(1+\bar{\chi})^2}. \tag{17}$$

At $x = L$, given the built-in boundary conditions $v(L) = v'(L) = 0$, the solution to equation (16) can be reduced to

$$v_{\max} = \frac{3P}{\kappa}\left[\frac{1}{\varphi^2} - \frac{\tanh\varphi}{\varphi^3}\right] \tag{18}$$

where

$$\varphi = \sqrt{\frac{3\kappa_{\mathrm{H}}}{\kappa}}, \tag{19}$$

$$\kappa_{\mathrm{H}} = \frac{\mu_0 A c H^2}{L}, \tag{20}$$

and κ is the elastic bending stiffness defined earlier. The term κ_{H} represents a field-induced stiffness. Note that in this derivation for S-MRE materials $\kappa_{\mathrm{H}} \propto H^2$.

To calculate $\bar{\chi}$, one appeals to effective medium theory. If the magnetization of the filler particles M_{m} can be written as $M_{\mathrm{m}} = \chi H$, where χ is the susceptibility of the soft-magnetic particles, assuming spherical shapes, the susceptibility of the composite $\bar{\chi}$ is therefore written as

$$\bar{\chi} \cong \frac{f\chi}{1 + 1/3(1-f)\chi} \tag{21}$$

where f is the volume fraction of magnetic material.

Recent work by Boczkowska *et al* [29] has investigated the spatial alignment of particle in Fe-based MREs with volume fractions of 1.5–33%. That work states that '[a] higher particle volume fraction (33 vol%) results in more complex particle arrangements, typical of isotropic three-dimensional networks of particles' and that 'for the highest volume fraction of particles (33% therein) an isotropic network is formed'. That work mentions the formations of chains and clusters of particles but specifically says that these chains occur increasingly at the lowest volume fractions studied (<11%). We have also begun investigating the spatial arrangement of particles in Fe- and BaM-based MREs using x-ray computed tomography. In addition to not seeing spatial alignment in Fe-based samples having ~30% particle volume fractions, we have not observed spatial alignment in BaM samples of similar particle volume fractions. Consequently, the use of the equation (21), typically reserved for random arrangements of particles, to describe the magnetic behavior of the material is warranted.

Since $\chi \gg 1$ for soft-magnetic materials

$$\bar{\chi} \cong \frac{3f}{(1-f)}, \tag{22}$$

yielding

$$c = \frac{27 f^3}{(1-f)(1+2f)^2}. \tag{23}$$

Figure 11 shows P versus $v_{\max}$ as predicted by equations (18)–(20) for the A–S material (lines) compared to data (symbols) at varying field strengths. The data are the same as those collected for the samples tested for figure 4(a). The prediction uses $\kappa = 27.0\,\mathrm{N\,mm^{-1}}$ as measured in experiments, $f = 30\%$, $L = 50$ mm, and $A = 5 \times 20\,\mathrm{mm^2}$. In figure 11, the $\mu_0 H = 0.09$ T (maximum field strength) data have been fitted to the model to determine $c = 2.2$. The prediction returns the elastic and large-field cases as expected and also models the intermediate field cases reasonably well (average error of 18.1% for data at all displacements and field strengths). The c value determined from the fit and equation (17) suggests that $\bar{\chi} \sim 2.2$, while the measured value of $\bar{\chi}$ determined from vibrating sample magnetometry varies between 8 at low fields and about 2 at about 80 $\mathrm{kA\,m^{-1}}$ and the calculated value of $\bar{\chi}$ from equation (22) is 1.3. There is reasonable agreement between the measured high-field susceptibility and the magnetoelastic response predicted by the current model; however, while qualitatively correct, equation (22) generally underestimates c.

5. Discussion

This paper defined four classes of MREs based on alignment–magnetization pairs and tested them in a cantilever bending

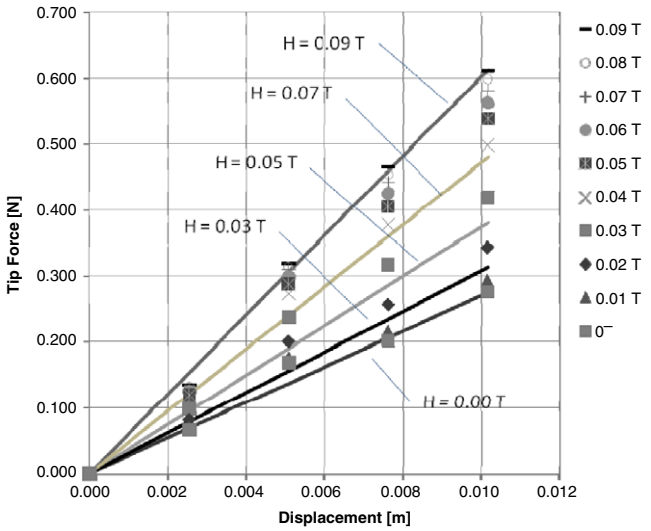

Figure 11. Tip force as a function of field and tip displacement for A–S material. The lines represent predictions made with equation (18) based on one adjustable parameter, c, which depends upon the magnetic susceptibility.

mode. Particle alignments were either unaligned (random) or aligned based on the curing process used. Particle magnetizations were either soft-magnetic (S-MRE) or hard-magnetic (H-MRE). Together, this created four classifications: A–H, A–S, U–H, and U–S.

Bending tests supported the authors' assertions that stark differences in response would exist among the four classes. Blocked force tests in a cantilever bending mode showed class A–H materials generated the highest magnetically-induced (partitioned from the elastic behavior) force (0.38 N), with classes U–S and A–S following with 0.37 N and 0.34 N, respectively, at $\mu_0 H = 0.09$ T. Class U–H showed only a maximum 0.04 N owing to the magnetic disorder inherent in the randomly aligned hard-magnetic particles.

Furthermore, experimental results highlighted the fact that while the A–H material was capable of free deflection and generated forces at its tip over the entire 0–10 mm deflection range, both S-MRE materials were incapable both of free deflection and, consequently, of generating forces at zero deflection. The H-MRE A–H material also showed higher magnetic work potential than the S-MRE materials and substantially more than the U–H H-MRE, all materials having similar magnetic particle volume fractions.

Experimental bending results and subsequent beam theory calculations yielded the magnitude of the internal magnetic moment, m_{H}, the driving actuation, in all four classes. These results showed that the S-MRE U–S and A–S cases behaved linearly with respect to displacement while the internal moment of the H-MRE A–H case remained relatively constant, highlighting a fundamental difference in the driving mechanisms between S- and H-MREs. H-MREs, driven by $\mathbf{T} = \mathbf{M} \times \mathbf{H}$, ideally maintain a constant internal moment $\mathbf{T}$ (especially for small deflections) while S-MREs, driven by demagnetizing effects that are based upon single- and multi-particle symmetries, scale with deformation since in the undeformed state $\mathbf{M}$ and $\mathbf{H}$ are parallel.

Two predictive models were developed around the two types of magnetic behavior. One employed an idealized distributed internal moment to capture the magnetic response of A–H H-MRE behavior (equations (5)–(8)) while the other was based upon the energy of demagnetization between particles in S-MREs (equations (9)–(23)). Both were coupled with Bernoulli–Euler beam theory to model elastic behavior. The distributed internal moment model of A–H H-MRE behavior, which had two fit parameters and no adjustable ones, agreed well with data over a range of tip deflections and applied field strengths (see figure 9). Furthermore, it predicted the free deflection and blocking-force-at-zero-deflection results seen experimentally. The demagnetization-based model of S-MRE cantilever bending also compared favorably to data, with results over a range of tip deflections and magnetic fields (see figure 11). With one adjustable parameter which can be independently determined from the magnetization, the demagnetization-based model accurately predicted the linear scaling of tip force with tip deflection.

While this work has focused on the variation in magnetic behavior across the four classes, figure 7 highlights variation in elastic response as well. In the figure, the A–S and U–S MREs show differing bending stiffnesses which one might initially associate with aligned or unaligned particle distributions. However, while particle alignment (or chaining) induced by curing in a magnetic field has been a paradigm of the MRE literature a more recent study has shown that at high volume fractions (including the 30% v/v used herein) MREs comprising 4–6 μm carbonyl iron show no alignment. The particles do not undergo wholesale motion to create chain-like structures. In addition, magnetization tests conducted by us on U–S and A–S samples show that the materials are magnetically isotropic (not shown) as well. Therefore, identifying the chain-like alignment typically associated with MREs as the causal factor in the difference in elastic bending behavior would not be accurate in this case. However, the difference in elastic response does suggest some level of structural difference between the two materials that bears examination.

Current investigations of MRE microstructures are limited to fractions of the total sample geometry [28]. These studies would not capture larger structures that percolate (or span) length scales of the order of the entire specimen. Additionally, no studies of the contact interaction between neighboring particles, attracted to each other locally during curing, have been performed. The particulate nature of MREs is important to remember since the mechanics of granular media identify anisotropic distribution of contacts, which would occur on a particle-to-particle length scale, as a source of variation in the bulk response [30]. To the best of our knowledge, studies of MRE behavior or structure in these two regimes, distribution of particle contacts and the percolation of aggregates of particles induced by curing in the presence of a magnetic field, have not been conducted in the MRE literature. We believe that further studies are clearly necessary and should focus on these two length scales.

6. Conclusions

With four material classes as proxies for material and magnetic symmetries, this work has shown the importance of differentiating classes of MRE behavior. This work has elucidated the significance of demagnetizing effects as a root cause of S-MRE behavior in bending and should further influence understanding of the MRE effect in research using S-MRE materials with a focus on improving ΔG. We have also shown the utility of using hard-magnetic particles to develop useful magnetic symmetries within the bulk which can, in turn, be used to provide actuation. Results of modeling have also highlighted field-dependent magnetic behavior characteristics m_H and κ_H, and an elasto-magnetic coupling factor φ that may prove useful in characterizing and designing devices with H- and S-MREs in cantilever bending applications.

Finally, the work highlights the ability of the A–H material to operate as a remotely powered actuator, a device controlled and powered without physical connections. Such devices are being assessed for use in *in situ* applications where physical connections are not possible but actuation, control, and possibly indefinite operation are required. While piezoelectric materials are a staple smart-material for actuation, the remotely powered aspect of these MREs transcends traditional piezoelectric capabilities. Furthermore, while magnetostrictives such as Terfenol-D may be powered remotely in a similar fashion, the range of bending deflections seen herein is well beyond the capabilities of the brittle Terfenol-D. Together these properties carve a unique niche in the field of smart materials for A–H MREs.

Acknowledgments

We would like to thank the National Science Foundation for support of this work through NSF CMMI no. 0927326.

References

[1] Ginder J M, Nichols M E, Elie L D and Tardiff J L 1999 Magnetorheological elastomers: properties and applications *Proc. SPIE* **3675** 131
[2] Borcea L and Bruno O 2001 On the magneto-elastic properties of elastomer–ferromagnet composites *J. Mech. Phys. Solids* **49** 2877
[3] Ginder J M, Clark S M, Schlotter W F and Nichols M E 2002 Magnetostrictive phenomena in magnetorheological elastomers *Int. J. Mod. Phys.* B **16** 2412
[4] Dorfmann A and Ogden R W 2003 Magnetoelastic modeling of elastomers *Eur. J. Mech.* A **22** 497
[5] Zhou G Y 2003 Shear properties of a magnetorheological elastomer *Smart Mater. Struct.* **12:1** 139
[6] Lokander M and Stenberg B 2003 Performance of isotropic magnetorheological rubber materials *Polym. Test.* **22** 245
[7] Lokander M and Stenberg B 2003 Improving the magnetorheological effect in isotropic magnetorheological rubber materials *Polym. Test.* **22** 677
[8] Lanotte L, Ausiano G, Hison C, Iannotti V, Luponio C and Luponio C Jr 2004 State of the art and development trends of novel nanostructured elastomagnetic composites *J. Optoelectron. Adv. Mater.* **6** 523
[9] Kankanala S V and Triantafyllidis N 2004 On finitely strained magnetorheological elastomers *J. Mech. Phys. Solids* **52** 2869
[10] Shen Y, Golnaraghi M F and Heppler G R 2004 Experimental research and modeling of magnetorheological elastomers *J. Intell. Mater. Syst. Struct.* **15** 27
[11] Lindroos T, Aalto S, Jarvinen E, Karna T, Meinander M and Kallio T 2007 Dynamic compression testing of a tunable spring element consisting of a magnetorheological elastomer *Smart Mater. Struct.* **16** 506
[12] Boczkowska A, Awietjan S F and Wroblewski R 2007 Microstructure-property relationships of urethane magnetorheological elastomers *Smart Mater. Struct.* **16** 1924
[13] von Lockette P, Koo J H, Lofland S E and Dermond M 2008 Dynamic characterization of bimodal particle mixtures in silicone rubber magnetorheological materials *Polym. Test.* **27** 931
[14] Zhang X, Peng W, Weijia S and Li W 2008 Analysis and fabrication of patterned magnetorheological elastomers *Smart Mater. Struct.* **17** 045001
[15] Deng H-X, Gong X-L and Wang L-H 2006 Development of an adaptive tuned vibration absorber with magnetorheological elastomer *Smart Mater. Struct.* **15** N111–6
[16] Nguyen T M and Elahinia M H 2005 A magnetoreological vibration isolator for hydraulic hybrid vehicles *Proc. ASME 2005 Int. Mechanical Engineering Congr. and Exposition* **IMECE2005-81355** p 185
[17] Zhou G Y and Wang Q 2005 Field-dependant dynamic properties of magnetorheological elastomer based sandwich beams *Proc. SPIE* **5760** 226
[18] Zhou G Y and Wang Q 2005 Use of magnetorheological elastomer for smart piezoelectric power actuator design and signal processing *Proc. SPIE* **5764** 411
[19] Zhou G Y and Wang Q 2005 Magnetorheological elastomer-based smart sandwich beams with nonconductive skins *Smart Mater. Struct.* **14** 1001–9
[20] Zhou G Y and Wang Q 2006 Use of magnetorheological elastomer in an adaptive sandwich beam with conductive skins. Part I: magnetoelastic loads in conductive skins *Inter. J. Solids Struct.* **43** 5386
[21] York D, Wang X and Gordaninejad F 2007 A new MR fluid-elastomer vibration isolator *J. Intell. Mater. Syst. Struct.* **18** 1221
[22] Wei H, Wereley N M, Chemouni L and Chen P C 2007 Sem-HActive linear stroke magnetorheological fluid-elastic helicopter lag damper *J. Guid. Control Dyn.* **30** 565
[23] Hu W and Werely N M 2008 Hybrid magnetorheological fluid-elastomeric lag dampers for helicopter stability augmentation *Smart Mater. Struct.* **17** 045021
[24] York D, Wang X and Gordaninejad F 2008 A new magnetorheological fluid-elastomer vibration isolator *Proc. SPIE* **6928** 69281D
[25] Opie S and Woosoon Y 2008 A tunable vibration isolator using a magnetorheological elastomer with a field induced modulus bias *IMECE 2007: Proc. ASME Int. Mechanical Engineering Congr. and Exposition* **IMECE2007-41505** p 99
[26] Lerner A A and Cunefare K A 2008 Performance of MRE-based vibration absorbers *Intell. Mater. Syst. Struct.* **19** 551
[27] Deng H-x and Gong X-l 2008 Application of magnetorheological elastomer to vibration absorber *Commun. Nonlinear Sci. Numer. Simul.* **13** 1938
[28] Boczkowska A, Awietjan S F, Wejrzanowski T and Kurzydłowski K J 2009 Image analysis of the microstructure of magnetorheological elastomers *J. Mater. Sci.* **44** 3135–40
[29] Brown W F 1962 *Magnetostatic Principles in Ferromagnetism* ed E P Wohlfarth (New York: Interscience)
[30] Peña A, García-Rojo R and Herrmann H 2007 Influence of particle shape on sheared dense granular media *Granular Matter* **9** 279–91